

Trajectory Manifold Optimization for Fast and Adaptive Kinodynamic Motion Planning

Yonghyeon Lee

Abstract—Fast kinodynamic motion planning is crucial for systems to effectively adapt to dynamically changing environments. Despite some efforts, existing approaches still struggle with rapid planning in high-dimensional, complex problems. Not surprisingly, the primary challenge arises from the high-dimensionality of the search space, specifically the trajectory space. We address this issue with a two-step method: initially, we identify a lower-dimensional trajectory manifold *offline*, comprising diverse trajectories specifically relevant to the task at hand while meeting kinodynamic constraints. Subsequently, we search for solutions within this manifold *online*, significantly enhancing the planning speed. To encode and generate a manifold of continuous-time, differentiable trajectories, we propose a novel neural network model, *Differentiable Motion Manifold Primitives (DMMP)*, along with a practical training strategy. Experiments with a 7-DoF robot arm tasked with dynamic throwing to arbitrary target positions demonstrate that our method surpasses existing approaches in planning speed, task success, and constraint satisfaction.

Index Terms—Movement primitives, kinodynamic planning, learning from demonstration, manifold learning, autoencoders, flow-based models

I. INTRODUCTION

Kinodynamic motion planning seeks to identify a trajectory that achieves a specified task while meeting various constraints such as joint, velocity, acceleration, torque limits, and avoiding self-collisions. Consider, for example, a 7-DoF robot arm tasked with throwing a ball into a target box. This requires the robot to accelerate and decelerate within these constraints to successfully throw the ball and then come to a stop within a set time frame. Now, suppose the target box unexpectedly moves after the robot has initiated its throwing motion. The robot must quickly adjust its trajectory to adapt to new task requirements while adhering to kinodynamic constraints. In such dynamically changing environments, *fast* kinodynamic motion planning is crucial for *adaptation*, which we aim to address in this paper.

The problem of kinodynamic planning has been explored through various methods including sampling, search, and optimization techniques [1], [2], [3], [4], [5], [6], [7], [8], [9], [10], [11], [12], [13], [14], [15], [16]. Despite progress, quickly finding solution trajectories that involve complex, nonlinear

Yonghyeon Lee was the beneficiary of an individual grant from CAINS supported by a KIAS Individual Grant (AP092701) via the Center for AI and Natural Sciences at Korea Institute for Advanced Study. Yonghyeon Lee is with the Center for AI and Natural Sciences (CAINS), Korea Institute for Advanced Study (KIAS), Seoul 08826, South Korea (e-mail: ylee@kias.re.kr). This work has been submitted to the IEEE for possible publication. Copyright may be transferred without notice, after which this version may no longer be accessible.

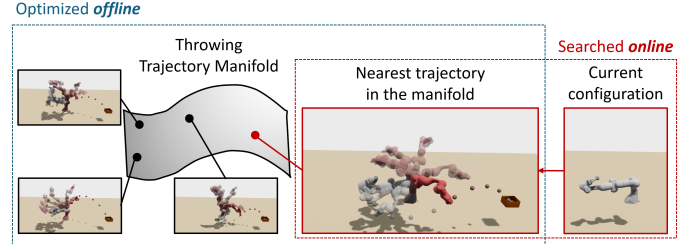


Fig. 1. Throwing trajectory manifold – which consists of task-completing trajectories that satisfy the kinodynamic constraints – is optimized *offline*, and given a current configuration, the nearest throwing trajectory can be quickly searched *online* within the manifold. The moment of the throw is depicted in deep red, preceded by gray and followed by transparent red.

dynamics and constraints remains a significant challenge, primarily due to the high dimensionality of the search space. For example, when the planning problem is formulated as an optimization and solved using direct collocation methods [17], the dimensionality increases linearly with the number of discretized time grid points, often reaching thousands of dimensions.

In contrast, consider how humans achieve rapid kinodynamic planning. Rather than exploring an entire, large trajectory space, humans are more likely to search through a much smaller space informed by specific motor patterns ingrained, for instance, in muscle memory related to the throwing motion. Building on this concept, we propose identifying a *trajectory manifold* – a lower-dimensional subspace consisting of task-relevant motions – *offline*, and then quickly searching for solutions *online* within this manifold, as illustrated in Fig. 1.

Encoding motions with mathematical models, commonly referred to as movement primitives, has been a key focus in the learning from demonstration literature [18], [19], [20], [21], where motions are typically obtained from human demonstrations. Recent advances in the Motion Manifold Primitives (MMP) framework are particularly relevant to our work, as they focus on encoding a manifold of trajectories that capture a diverse set of motions [22], [23], [24]. By incorporating kinodynamic planning algorithms to generate demonstration trajectory data – unlike previous works that predominantly relied on human demonstration data – the MMP framework can be seamlessly adapted for our purposes.

However, existing MMPs do not take into account kinodynamic constraints, leading to trajectories that severely violate them. A common solution in deep learning is to introduce an additional loss term during training to enforce constraint satisfaction. However, the discrete-time trajectory represen-

tations used in current MMP models are not differentiable with respect to time, making it challenging to implement differentiable losses for kinodynamic constraints.

In this context, our contributions are two-fold. The first contribution is *Differentiable Motion Manifold Primitives (DMMP)*, a novel neural network architecture designed to encode and generate a manifold of continuous-time trajectories differentiable in time. Generalizing conventional movement primitives [20], [25], our DMMP model is constructed as a linear basis function model, with the basis and coefficients being neural network functions of latent and time variables, respectively.

The second contribution is a practical four-step training strategy for DMMP (see Fig. 4; details are provided in section IV). Initially, we collect multiple trajectories for each task parameter by solving optimization problems with diverse random initializations and seeds. Next, we fit these trajectories into a differentiable motion manifold. We then develop a task-conditioned latent flow model. Finally, we freeze the latent flow and fine-tune the manifold to ensure that generated trajectories achieve the tasks and comply with kinodynamic constraints.

We present a case study on a dynamic throwing task using a 7-DoF robot arm, which exemplifies challenging kinodynamic motion planning problems. To throw beyond the workspace limits, the robot must adopt a preparatory posture, such as pulling its arm back, and fully utilize its velocity limits. This requires the entire joint trajectory to be optimized, not just a throwing phase, while considering kinodynamic constraints, making the problem highly complex.

We compare our DMMP with conventional trajectory optimization methods, such as parametric curve optimization, as well as existing MMPs, evaluating task success rates, constraint satisfaction rates, and planning times. Our findings demonstrate that our method generates trajectories much more quickly than traditional trajectory optimization, with significantly higher success and constraint satisfaction rates compared to existing MMPs.

II. RELATED WORKS

A. Kinodynamic Motion Planning

Kinodynamic planning combines the search for a collision-free path with the system’s inherent dynamics, ensuring that the resulting trajectory is feasible [1]. Many sampling, search, and optimization-based methods have been developed [2], [3], [4], [5], [6], [7], [8], [9], [10], [11], [12], but it is still difficult to perform real-time kinodynamic planning for problems with highly nonlinear dynamics and constraints. Some recent efforts have focused on using deep neural networks for fast planning. Learning-based modules have been introduced to improve the planning speed of the popular sampling-based method, the kinodynamic RRT* [13], [14]. Meanwhile, end-to-end neural network planners have been developed [15], [16], though without considering dynamic constraints.

Of particular relevance to our approach is the Constrained Neural Motion Planning with B-splines (CNP-B), which generate continuous-time trajectories parametrized by

B-splines [26]. The key difference is that our model, a type of generative model, can encode a manifold of continuous-time trajectories, enabling it to generate multiple trajectories for a given task, while CNP-B generates a single optimal trajectory.

B. Motion Manifold Primitives

Recently, task-conditioned generative models that can generate multiple trajectories for each task parameter have been explored. Given the high dimensionality of trajectory data – often represented as a sequence of configurations –, a common approach leverages the manifold hypothesis and employs an encoder-decoder framework to learn a lower-dimensional manifold of trajectories [22], [23], [24]. Initial methods used conditional autoencoder architectures, where decoders took both latent variables and task parameters as inputs [22], [23]. Later, Motion Manifold Flow Primitives (MMFP) demonstrated that first identifying lower-dimensional motion manifolds and then learning flow models within these latent spaces can more effectively capture complex conditional distributions [24].

However, these existing approaches rely on discrete-time trajectory representations, which prevents the generated trajectories from being differentiated over time. This makes it challenging to design loss functions that enforce kinodynamic constraints. Recently, motion manifold primitives utilizing user-defined parametric curve models, which are continuous-time trajectory representations that enable time differentiation, have been introduced [27], focusing on simpler, unconditioned trajectory modeling. In contrast, our approach learns a manifold of continuous-time, differentiable trajectories using more expressive neural network models, without relying on predefined parametric curve models.

III. PRELIMINARIES: MOTION MANIFOLD PRIMITIVES

This section reviews existing discrete-time MMP methods [22], [23], [24] to clarify their limitations. We begin this section with notations and common assumptions used in these works. Let $Q \subset \mathbb{R}^n$ be an n -dimensional configuration space and denote a configuration by q . A demonstration trajectory is given as a sequence of configurations $(q_1, \dots, q_L) \in Q^L$. We denote a task parameter by τ and its space by \mathcal{T} , which is assumed to be compact. For example, [23] solved a water-pouring task where the position of the cup, the initial pose of the bottle, and the amount of water were considered as τ , while [24] treated a text embedding vector as τ for a language-guided trajectory generation task.

We are given a dataset of task-trajectory pairs: for each task parameter $\tau_i \in \mathcal{T}$, where $i = 1, \dots, M$, there are N_i trajectories $\{(q_{ij,1}, \dots, q_{ij,L}) \in Q^L\}_{j=1}^{N_i}$. The goal is to learn a model that maps an input task parameter $\tau \in \mathcal{T}$ to a set of trajectories that fit the distribution of demonstrated trajectories. One naive approach would be to fit a probability density model directly in the trajectory space; however, due to the high dimensionality and limited dataset size, the performance is often suboptimal. To address this issue, MMPs commonly adopt an autoencoder framework for dimensionality reduction.

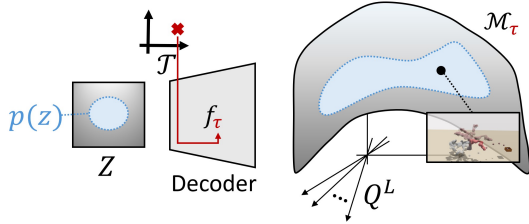


Fig. 2. The decoder f_τ in MMPs [22], [23] maps the latent space Z to the manifold \mathcal{M}_τ embedded in the discrete-time trajectory space Q^L ; the latent prior distribution $p(z)$ is consequently mapped to the density in \mathcal{M}_τ .

The autoencoder framework is widely recognized as an effective method for learning a lower-dimensional data manifold embedded in a high-dimensional data space [28], [29], [30], [31], [32], [33], [34], [35]. Earlier works on MMPs [22], [23] employ conditional autoencoder architectures to incorporate task parameters. Specifically, they consider a pair of mappings: an encoder $g : Q^L \rightarrow Z$ and a decoder $f : \mathcal{T} \times Z \rightarrow Q^L$, where $Z = \mathbb{R}^m$ represents the latent space (m is set to be much smaller than the dimension of the trajectory space $L \times \dim(Q)$). These mappings, approximated using deep neural networks, are trained to minimize the reconstruction loss:

$$\min_{g,f} \frac{1}{M} \sum_{i=1}^M \frac{1}{N_i} \sum_{j=1}^{N_i} \|f(\tau_i, g(q_{ij, \text{traj}})) - q_{ij, \text{traj}}\|^2, \quad (1)$$

where $q_{ij, \text{traj}} = (q_{ij,1}, \dots, q_{ij,L})$ and $\|\cdot\|$ is some suitable norm on the trajectory space. Other variations, such as the evidence lower bound (ELBO) loss in variational autoencoders [36], can essentially be interpreted as minimizing the above reconstruction loss with additional regularization terms.

Given a sufficiently low reconstruction error and mild regularity conditions on the decoder f (such as injectivity and immersion), the image of the decoder for a fixed τ , denoted by $f_\tau(z) := f(\tau, z)$, can be interpreted as an m -dimensional manifold of trajectories $\mathcal{M}_\tau := f_\tau(Z)$, embedded in the high-dimensional trajectory space Q^L , as visualized in Fig 2. Additionally, in \mathcal{M}_τ , the regions where the data lie should be specified. For this purpose, we can fit a probability density model $p(z)$ in the latent space Z , so that f_τ maps $p(z)$ to the density in \mathcal{M}_τ . [22] uses a Gaussian prior distribution for $p(z)$, whereas [23] fits a Gaussian mixture model to capture multi-modality.

More recently, [24] pointed out that the conditional autoencoder architecture shows suboptimal performance when the motion manifold or distribution changes dramatically depending on the task variable τ , as a single decoder network $f(\tau, z)$ struggles to capture such complex functions. Instead, they proposed a two-step approach: first, an unconditional autoencoder model is used to learn the manifold of trajectories, and then a sufficiently expressive model (e.g., diffusion models, flow models) is employed in the latent space to learn the complex task-conditioned probability distribution, demonstrating improved performance.

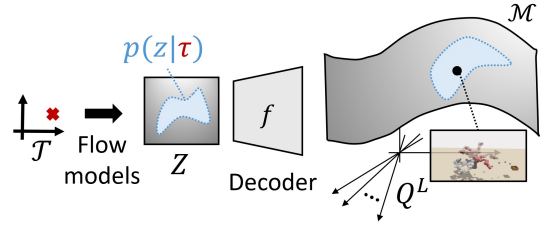


Fig. 3. The decoder f in MMFP [24] maps the latent space Z to the manifold \mathcal{M} of all trajectories embedded in the discrete-time trajectory space Q^L ; the latent task-conditioned distribution $p(z|\tau)$ is consequently mapped to the task-conditioned density in \mathcal{M} .

Specifically, an encoder $g : Q^L \rightarrow Z$ and a decoder $f : Z \rightarrow Q^L$ are trained by minimizing

$$\min_{g,f} \frac{1}{M} \sum_{i=1}^M \frac{1}{N_i} \sum_{j=1}^{N_i} \|f(g(q_{ij, \text{traj}})) - q_{ij, \text{traj}}\|^2, \quad (2)$$

then a task-conditioned probability density model $p(z|\tau)$ is fitted in Z , by using the encoded data points: $\{\tau_i, \{z_{ij}\}_{j=1}^{N_i}\}_{i=1}^M$ where $z_{ij} = g(q_{ij, \text{traj}})$. The decoder f then parameterizes a manifold of all trajectories, and $p(z|\tau)$ specifies the latent coordinates z of trajectories for a given τ . [24] used flow models for $p(z|\tau)$ and train them with recent flow matching algorithms [37] – which we adopt later in our framework – and termed them Motion Manifold Flow Primitives (MMFP); see Fig. 3 for illustrations.

We could apply these approaches to our problem by first collecting a set of trajectories using any kinodynamic motion planning algorithm and treating them as discrete-time trajectories. However, there are two major limitations when tackling challenging kinodynamic planning tasks (e.g., the throwing task discussed later in the experiments). First, existing MMPs simply fit the collected trajectories by interpolating them, meaning that newly generated trajectories are not guaranteed to satisfy kinodynamic constraints and may violate them. Second, since the set of task parameters seen during training is limited (as collecting trajectories for all feasible τ is infeasible), their performance may not reliably generalize to unseen task parameters. In the subsequent section, we propose an additional trajectory manifold optimization step with a novel primitive model, differentiable motion manifold primitives, which addresses all the aforementioned challenges and significantly improves the overall performance of the primitive models.

IV. DIFFERENTIABLE MOTION MANIFOLD PRIMITIVES

We begin this section with assumptions, notations, and problem definitions. The same notations from section III are used for the configuration $q \in Q$ and the task parameter $\tau \in \mathcal{T}$. We consider a fixed terminal time T and denote a smooth trajectory by $q(t)$ for $t \in [0, T]$. Sometimes, an additional variable is needed to fully represent a motion. We denote this variable as η . For example, in the throwing task, the throwing time $\eta \in (0, T)$ must be determined so that the object is thrown at $q(\eta) \in Q$.

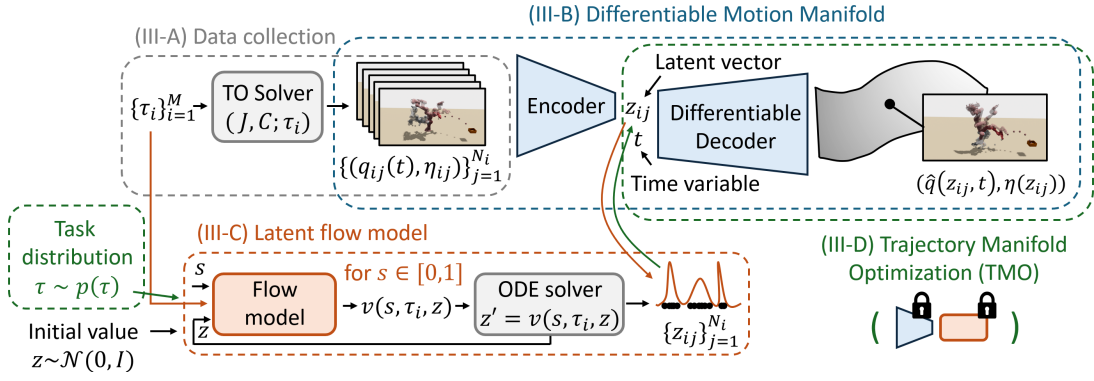


Fig. 4. Illustration of the overall training pipeline for the trajectory manifold. First, given a finite set of task parameters, we collect multiple, diverse trajectories for each task parameter using any existing Trajectory Optimization (TO) method. Second, we fit a Differentiable Motion Manifold (DMM) consisting of an encoder and a differentiable decoder – by differentiable, we mean differentiable in time. Third, we learn a flow-based, task-conditioned distribution in the latent space. Lastly, we fine-tune the trajectory manifold by optimizing the decoder – where we freeze the pre-trained encoder and latent flow model – to ensure that the generated trajectories achieve the tasks and comply with kinodynamic constraints for all task parameters randomly sampled from the task distribution.

Instead of being provided with demonstration trajectories, we assume that a task-dependent objective function $J(q(\cdot), \eta; \tau)$ – which is a functional of $q(t)$ – is given. Second, we assume that kinodynamic constraints, e.g., self-collisions, joint, velocity, acceleration, jerk limits, and torque limits, are given by $C(q, \dot{q}, \ddot{q}, \ddot{q}) \leq 0$, where $C(q, \dot{q}, \ddot{q}, \ddot{q}) \in \mathbb{R}^k$ is vector-valued and differentiable. Lastly, we assume that there are multiple global optimal motions $(q(t), \eta)$ or good enough local optimal motions for each task τ . For example, given a target position, there can be multiple possible throwing trajectories. Then, our goal is to learn or optimize a neural network model that, given an arbitrary task parameter input $\tau \in \mathcal{T}$, can generate multiple motions $(q(t), \eta)$ that are optimal and meet the given constraints.

Our framework consists of four steps. First, we collect multiple optimal trajectories by solving trajectory optimizations for each τ using different initializations and seeds in section IV-A. Using these trajectories, we fit a differentiable motion manifold in section IV-B. In section IV-C, we train a task-conditioned motion distribution by learning a flow-based model in the latent coordinate space of the learned motion manifold. Lastly, in section IV-D, we fine-tune the motion manifold using the given objective function J and constraints C . The overall pipeline is visualized in Fig. 4.

A. Data Collection via Trajectory Optimizations

The goal of this section is to collect multiple trajectories for each τ , which will be used in the subsequent motion manifold learning. Since it is infeasible to collect data for all $\tau \in \mathcal{T}$, we first select a finite subset of \mathcal{T} , denoted by $\mathcal{T}_s = \{\tau_i\}_{i=1}^M \subset \mathcal{T}$, that approximately covers \mathcal{T} . For each τ_i , we solve the following optimization:

$$\min_{q(t), \eta} J(q(\cdot), \eta; \tau_i) \quad (3)$$

such that $C(q(t), \dot{q}(t), \ddot{q}(t), \ddot{q}(t)) \leq 0$ for all $t \in [0, T]$. Any optimization algorithm (or any planning algorithm) can be used; by employing different random seeds, initializations, or

any inherent randomness in algorithms, we solve this problem multiple times to obtain diverse solution trajectories.

In this paper, adopting the via-point movement primitives [25], we use the following parametric curve model and perform the optimization in the parameter space:

$$q(t) = q_0 + (q_T - q_0)(3 - 2s)s^2 + s^2(s - 1)^2\Phi(s)w, \quad (4)$$

where $s = t/T$, $q_0, q_T \in Q \subset \mathbb{R}^n$, $\Phi(s) = [\phi_1(s), \dots, \phi_B(s)] \in \mathbb{R}^{1 \times B}$ – where $\phi_i(s) = \exp(-B^2(s - \frac{i-1}{B-1})^2)$ and B is the number of basis functions –, and $w \in \mathbb{R}^{B \times n}$. We note that the coefficients are carefully chosen so that $q(0) = q_0$, $q(T) = q_T$, and $\dot{q}(0) = \dot{q}(T) = 0$. We consider q_0, q_T, w as parameters for $q(t)$.

To collect diverse trajectories, we randomly initialize q_0, q_T and solve (3). We iterate this process multiple times with different random seeds. As a result, for each τ_i , we have multiple motions $\{(q_{ij}(t), \eta_{ij})\}_{j=1}^{N_i}$ where $q_{ij}(t)$ is given by (4) with $(q_0)_{ij}, (q_T)_{ij}$ and w_{ij} . At this stage, the speed of solving the optimization problem is not crucial, as it only needs to be done once offline to collect good data. During actual control, there is no need to solve this optimization problem again.

B. Learning Differentiable Motion Manifold

In this section, we propose a method to train a manifold of continuous-time, differentiable trajectories using the dataset $\{(q_{ij}(t), \eta_{ij})\}_{j=1}^{N_i}$. The key idea is to design the decoder – which outputs a discretized trajectory in the discrete-time MMPs – to take time as an additional input and produce a configuration as a function of time. A similar technique can be found in 3D modeling, where 3D spatial coordinates are used as an additional input to the shape latent code [38].

Specifically, we consider two mappings, an encoder g and decoder f , and an m -dimensional latent space $Z = \mathbb{R}^m$. The encoder g takes a discretized trajectory $(q_1, \dots, q_L) \in Q^L$ and η as inputs and outputs a latent value $z \in Z$, i.e., $g((q_1, \dots, q_L), \eta) = z$. The decoder f takes the latent value z and time variable t as inputs and outputs a configuration in

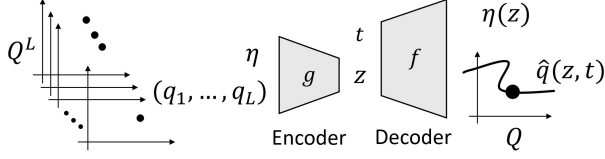


Fig. 5. The encoder takes $(q_1, \dots, q_L) \in Q^L$ and η and outputs the latent value z ; the decoder maps z and time variable t to a configuration $\hat{q}(z, t) \in Q$ and $\eta(z)$.

Q and η , i.e., $f(z, t) = (\hat{q}(z, t), \eta(z))$ – note η only depends on z . The decoder $f(z, t)$ is differentiable in t , and we call f a differentiable decoder; see Fig. 5.

The encoder and decoder are approximated with deep neural networks, denoted by g_α and $f_\beta = (\hat{q}_\beta, \eta_\beta)$, respectively, with parameters α, β , and trained to minimize the following loss function:

$$\mathcal{L}_{\text{recon}}(\alpha, \beta) := \frac{1}{M} \sum_i \frac{1}{N_i} \sum_j \|\hat{q}_\beta(z_{ij}, t) - q_{ij}(t)\|_{c(t)}^2 + \|\eta_\beta(z_{ij}) - \eta_{ij}\|^2, \quad (5)$$

where $z_{ij} = g_\alpha((q_{ij}(t_1), \dots, q_{ij}(t_L)), \eta_{ij})$, $t_l = \frac{l-1}{L-1}T$ for $l = 1, \dots, L$, and $\|\delta(t)\|_{c(t)}^2 := \int_0^T c(t)\delta^T(t)\delta(t)dt$ for some positive function $c(t) > 0$. The positive function $c(t)$ is introduced to fit more accurately on important parts along the time axis. For example, in the throwing task, the time around the throwing moment η should be given more weight.

Similar to the discrete MMP cases, given a sufficiently low-dimensional latent space Z and the injective immersion conditions on $\hat{q}_\beta : z \mapsto \hat{q}_\beta(z, \cdot)$, we can interpret the set of trajectories $\{\hat{q}_\beta(z, \cdot) | z \in Z\}$ as an m -dimensional differentiable manifold of trajectories [33], [30], which we refer to as the *Differentiable Motion Manifold (DMM)*.

Any neural network model can be employed for f_β . In this work, adopting ideas from deep operator learning [39], we propose a neural network architecture for \hat{q}_β based on the linear basis function model that offers better memory and computation efficiency:

$$\hat{q}_\beta(z, t) = \sum_{b=1}^{N_b} \psi_\beta^b(z) \theta_\beta^b(t), \quad (6)$$

where $\psi_\beta^b : Z \rightarrow \mathbb{R}$ and $\theta_\beta^b : \mathbb{R} \rightarrow \mathbb{R}^n$ for $b = 1, \dots, N_b$ – where N_b is the number of basis functions – are neural networks parametrized by β . With this model, calculating time derivatives of \hat{q} doesn't require differentiating ψ , reducing computational costs. Additionally, when inferring a single trajectory over time with a fixed z , we need to store only $\psi(z)$ instead of the full neural network parameters of ψ , which enhances memory efficiency.

C. Latent Flow Learning

This section introduces how to fit a task-conditioned density model $p(z|\tau)$ in the latent space of the learned differentiable motion manifold, by adopting the latent flow learning from MMFP [24]. Let z_{ij} denote a latent value of $(q_{ij}(t), \eta_{ij})$

encoded by the trained encoder g_α from the previous section. Then, we have a dataset of task-latent values $(\tau_i, \{z_{ij}\}_{j=1}^{N_i})_{i=1}^M$. Our goal is to train a task-conditioned latent probability density model $p(z|\tau)$ so that we can sample z given τ and then generate a motion by using the trained decoder, i.e., $z \mapsto f_\beta(z, \cdot)$.

The distribution $p(z|\tau)$ can be arbitrarily complex, e.g., it may have multiple modes and disconnected supports. Simple density models cannot fit $p(z|\tau)$, therefore, we use a sufficiently expressive deep generative model, specifically a flow-based model [40], [37].

In the latent space Z , consider a neural network velocity field $v_\gamma(s, \tau, z)$ parametrized by γ conditioned on s, τ for $s \in [0, 1]$ and an Ordinary Differential Equation (ODE):

$$\frac{dz}{ds} = v_\gamma(s, \tau, z). \quad (7)$$

Given a Gaussian prior distribution $p_0(z)$, we model $p_\gamma(z|\tau)$ as a pushforward of p_0 by the flow of v_γ . For example, to sample from $p_\gamma(z|\tau)$, we first sample from p_0 and solve the ODE from $s = 0$ to $s = 1$. We use the flow matching [37] to train v_γ , a simulation-free approach that is much more efficient than the conventional maximum log-likelihood method.

Consequently, by sampling from $z \sim p_\gamma(z|\tau)$ and using the differentiable decoder as $z \mapsto f_\beta(z, \cdot)$, we can generate motions for τ . We call this *Differentiable Motion Manifold Flow Primitives (DMMFP)*.

D. Trajectory Manifold Optimization

Trajectories generated by DMMFP are not guaranteed to satisfy the kinodynamic constraints. Additionally, because the dataset only includes a finite set of task parameters $\{\tau_i\}_{i=1}^M$, performance for unseen $\tau \in \mathcal{T}$ is also not guaranteed. In this section, we propose a trajectory manifold optimization to fine-tune the manifold, ensuring that generated trajectories not only achieve the tasks for all $\tau \in \mathcal{T}$ but also comply with kinodynamic constraints.

Specifically, let g_α , f_β , and p_γ be pre-trained encoder, decoder, and latent flow. Our key strategy is to fine-tune the decoder parameter β while fixing the encoder and flow parameters α, γ . One may reasonably ask why not fine-tune all the parameters (α, β, γ) simultaneously. While this is possible, it requires gradient backpropagation through the latent values sampled via the flow. Consequently, the entire computation graph from the ODE simulation must be traversed, which is computationally very expensive and significantly prolongs the training process. We only fine-tune the decoder parameters, as this is both efficient and sufficient to modify the motion manifold.

Specifically, let $U(S)$ be a uniform distribution on a set S . We then define a task loss as follows:

$$\mathcal{L}_{\text{task}}(\beta) := \mathbb{E}_{t, \tau, z} [J(\hat{q}_\beta(z, \cdot), \eta_\beta(z); \tau) + W^T (\text{ReLU}(C(t, z, \beta)))^2], \quad (8)$$

where the expectation with t, τ, z is taken over their respective distributions $t \sim U([0, T]), \tau \sim U(\mathcal{T}), z \sim p_\gamma(z|\tau)$, and $C(t, z, \beta)$ is defined as

$$C(\hat{q}_\beta(z, t), \frac{\partial}{\partial t} \hat{q}_\beta(z, t), \frac{\partial^2}{\partial t^2} \hat{q}_\beta(z, t), \frac{\partial^3}{\partial t^3} \hat{q}_\beta(z, t)) \in \mathbb{R}^k, \quad (9)$$

where $W \in \mathbb{R}^k$ is a positive weight vector. The first term enforces task success, and the second term ensures constraint satisfaction. We note that the task loss is averaged over all possible task parameters sampled from $U(\mathcal{T})$, improving generalization performance. Additionally, incorporating the reconstruction loss defined in equation (5) but with a fixed α , we minimize the following composite loss function:

$$\mathcal{L}(\beta) = w_{\text{recon}} \mathcal{L}_{\text{recon}}(\beta) + \mathcal{L}_{\text{task}}(\beta), \quad (10)$$

where w_{recon} is a positive weight parameter. We call this finetuning process *Trajectory Manifold Optimization (TMO)*.

V. CASE STUDY: DYNAMIC THROWING WITH A 7-DOF ROBOT ARM

In this section, we demonstrate the effectiveness of our algorithms for fast and adaptive kinodynamic planning with the dynamic throwing task using the 7-DoF Franka Panda robot arm. This involves solving a non-trivial kinodynamic optimization problem with nonlinear objectives and constraints, where the limits must be fully utilized. The solution process is highly dependent on initial conditions and can be time-consuming, making it an ideal example to showcase the effectiveness of our method. This will become more evident as the problem description is introduced below.

As shown in Fig. 6, the position of the target box is considered as the task parameter. We define $\tau = (r \cos \theta, r \sin \theta, h) \in \mathbb{R}^3$. When training motion manifold primitives, we assume $\theta = 0$, since if $\theta \neq 0$, we can simply rotate the first joint by θ for the generated trajectories, leveraging the rotational symmetry. If the target box is too close to the robot, there is no need to throw an object. Therefore, the task parameter space is defined as $\mathcal{T} := \{(r, 0, h) \mid r \in [1.1, 2.0], h \in [0.0, 0.3]\}$. The object is assumed to be released from the gripper immediately when the gripper opens, and thereafter, the object is assumed to be in free fall. The throwing time is considered as an additional variable $\eta \in [0, T]$ where the total time is $T = 5$. Thus, given a joint trajectory $q(t)$, the throwing phase – where the robot releases the object – is $(q(\eta), \dot{q}(\eta))$.

Objective function. We are assumed to be given kinematic and mass-inertial parameters of the robot arm and the relative position of the object to the gripper while holding it. Let $T_{sb} : Q \rightarrow \text{SE}(3)$ be the forward kinematics of the robot's end-effector frame, where $T_{sb}(q) = (R_{sb}(q), t_{sb}(q)) \in \text{SO}(3) \times \mathbb{R}^3$ is the end-effector frame described in the fixed frame $\{s\}$. Let $p_b \in \mathbb{R}^3$ be the relative position of the object described from the end-effector frame, then, when the robot is at a joint configuration q , the object position described in the fixed frame is given as

$$p_s(q) = R_{sb}(q)p_b + t_{sb}(q). \quad (11)$$

Let $J_b : Q \rightarrow \mathbb{R}^{6 \times 7}$ be the end-effector body Jacobian so that $(\omega_b, v_b) = J_b(q)\dot{q}$ is the body velocity. We note that

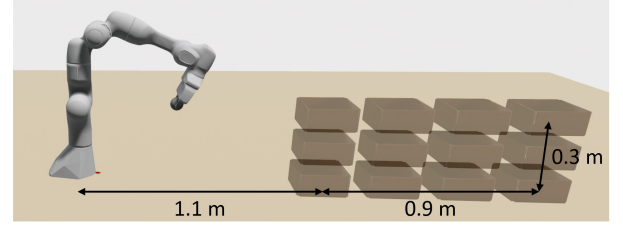


Fig. 6. Task parameter space \mathcal{T} , a set of positions of the target box.

$[\omega_b] = R_{sb}^T(q)\dot{R}_{sb}(q)$ – where $[a]$ is a 3×3 skew symmetric matrix such that $[a]_{12} = -a_3, [a]_{13} = a_2, [a]_{23} = -a_1$ for $a = (a_1, a_2, a_3)$ – and $v_b = R_{sb}^T(q)\dot{t}_{sb}(q)$. Given a joint velocity \dot{q} , the velocity of the object is then given as

$$\begin{aligned} \dot{p}_s(q) &= \dot{R}_{sb}(q)p_b + \dot{t}_{sb}(q) = R_{sb}(q)[\omega_b]p_b + R_{sb}(q)v_b \\ &= \begin{bmatrix} -R_{sb}(q)[p_b] \\ R_{sb}(q) \end{bmatrix} J_b(q)\dot{q}. \end{aligned} \quad (12)$$

Consequently, the position and velocity of the object at the moment of the throw are given by $(p_s(q(\eta)), \dot{p}_s(q(\eta)))$. Then, using the free-fall formula, we can compute the trajectory of the thrown object and measure how far it deviates from the target box.

The objective function $J(q(\cdot), \eta; \tau)$ is defined as the sum of two terms:

$$J(q(\cdot), \eta; \tau) = J_{\text{task}}(q(\cdot), \eta; \tau) + w_1 \frac{1}{T} \int_0^T \|\ddot{q}(t)\|^2 dt, \quad (13)$$

with a positive weight parameter w_1 . The first term is the squared position error, which will be explained in detail soon, while the second term regularizes the motion to have small jerks. The task objective function $J_{\text{task}}(q(\cdot), \eta; \tau)$ is defined as the square of the position error between the object and the target box at the moment the object passes through the z -coordinate of the target box. Specifically, recall that the trajectory of the thrown object after Δt has passed is given by

$$p_s(q(\cdot), \eta, \Delta t) = p_s(q(\eta)) + \dot{p}_s(q(\eta))\Delta t - \frac{1}{2} \begin{bmatrix} 0 \\ 0 \\ g \end{bmatrix} (\Delta t)^2,$$

where $g = 9.81 \text{ m/s}^2$ is the gravitational acceleration. Denote by Δt^* the larger of the two solutions to the quadratic equation below, as the object must enter the target box while falling:

$$(p_s(q(\eta)))_3 + (\dot{p}_s(q(\eta)))_3 \Delta t - \frac{1}{2} g (\Delta t)^2 - \tau_3 = 0, \quad (14)$$

where a_3 represents the third, or z -component of $a \in \mathbb{R}^3$. Then the task objective is

$$J_{\text{task}}(q(\cdot), \eta; \tau) := \|p_s(q(\cdot), \eta, \Delta t^*) - \tau\|^2. \quad (15)$$

Kinodynamic constraints. Additionally, the following kinodynamic constraints are considered: (i) limits on joint position, velocity, acceleration, and jerk; (ii) limits on end-effector linear and angular velocities; (iii) joint torque limits; (iv) limits on the minimum distance between links to avoid self-collision, computed by representing each link with collision capsules.

We note that since we have equations for the dynamics of the robot arm:

$$f = M(q)\ddot{q} + c(q, \dot{q}) + h(q), \quad (16)$$

where f is the joint torque vector, $M(q)$ is the mass matrix, $c(q, \dot{q})$ is the Coriolis force vector, and $h(q)$ is the gravitational force vector, we can express the torque in terms of q , \dot{q} , and \ddot{q} . Therefore, all the inequality constraints can be concatenated and expressed as follows:

$$C(q, \dot{q}, \ddot{q}, \ddot{q}) \leq 0, \quad (17)$$

with a vector-valued function $C(q, \dot{q}, \ddot{q}, \ddot{q}) \in \mathbb{R}^k$ ($k = 7 \times 5 + 2 + 7 + 1$). To give a safe margin, we add an offset of 0.01 to the limit size. For example, in the case where $|\dot{q}| \leq \dot{q}_{\max}$, $C(q, \dot{q}, \ddot{q}, \ddot{q}) := |\dot{q}| - \dot{q}_{\max} + 0.01 \times \dot{q}_{\max}$. For the minimum collision distance, we set a margin of 0.05 m. All limits are based on the official documentation for the Franka Panda, except for the end-effector velocity limits. We have doubled the typical end-effector velocity limits, enabling the Franka robot to throw objects up to 2 meters. Without this adjustment, the robot would not achieve sufficient throwing distance, while shorter throws would be too trivial.

We consider the trajectory optimization problem summarized by the objective function (13) and constraints (17). In general, trajectory optimization requires simultaneous optimization of the control input and state trajectory, along with enforcing forward dynamics constraints or using shooting methods with dynamic programming. On the other hand, our problem can be solved relatively much simply. We only need to optimize the joint trajectory $q(t)$, since we have the analytic inverse dynamics equations (16), i.e. $q(t)$ uniquely defines the control input trajectory.

Nevertheless, to throw an object far, the robot must fully utilize its Cartesian velocity limits, accelerating to the desired speed within the throwing time and decelerating within the time constraints. This process requires effective use of the entire arm length and momentum, making it a challenging optimization problem. It is highly sensitive to initial conditions, and even when a solution is found, the computation is time-consuming. The farther the object needs to be thrown, the longer it takes to compute the solution. We found that outside the task space \mathcal{T} , where $r > 2.0$ and $h > 0.3$, our optimization solver was unable to find solution trajectories due to these constraints. Therefore, this example is highly suitable for demonstrating the effectiveness of our learning-based fast kinodynamic planning algorithms.

Implementation details. In the norm $\|\cdot\|_{c(t)}$ of trajectory space, used in equation (5), we set $c(t) = \exp(-4(t - \eta)^2)$ to better fit the trajectory near the throwing time η . In the linear basis function model in equation (6), we set $N_b = 100$. Throughout, we use fully connected neural networks with GELU activation functions for each module in the motion manifold primitives, each consisting of approximately 4 to 6 layers and around 1024 nodes per layer (these specifics do not significantly impact the results). The finite subspace of \mathcal{T} used in optimization (3) is $\mathcal{T}_s := \{(r, 0, h) \mid r \in \{1.1, 1.2, \dots, 1.9, 2.0\}, h \in \{0.0, 0.1, 0.2, 0.3\}\}$. Forward kinematics, inverse dynamics, objective functions, and

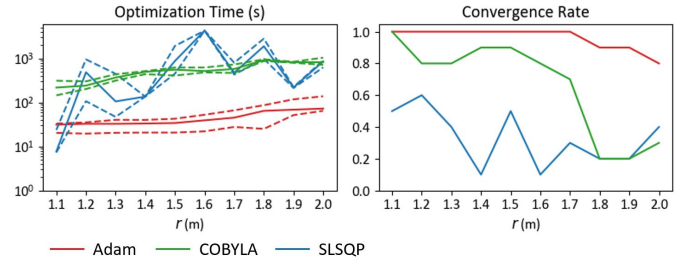


Fig. 7. Quartiles of the optimization times and convergence rates as functions of $r \in [1.1, 2.0]$, where the target box position is $\tau = (r, 0, 0)$. The quartiles are computed using only the successful cases from 10 optimization attempts.

constraints are all implemented using the deep learning library PyTorch in Python, with gradients computed through automatic differentiation. When solving the latent space ODE $z' = v_\gamma(s, \tau, z)$ for $s \in [0, 1]$ (7), we set $ds = 0.1$ and use the Euler method. Choosing ds too small increases the sampling time significantly, while setting it too large reduces accuracy. Empirically, $ds = 0.1$ is found to provide a good balance.

A. Data Collection via Trajectory Optimizations

In this section, we demonstrate how the time required for trajectory optimization in the throwing tasks varies with the target box position, followed by the dataset collection process and its statistics, which are used for learning DMMP. The trajectory optimization problem can be written as follows:

$$\min_{q_0, q_T, w, \eta} J(q_0, q_T, w(\cdot), \eta; \tau), \quad (18)$$

where $q_0, q_T, w(\cdot)$ is from (4) and $J(q(\cdot), \eta; \tau)$ is from (13), such that

$$C(q_{q_0, q_T, w}(t), \dot{q}_{q_0, q_T, w}(t), \ddot{q}_{q_0, q_T, w}(t), \ddot{q}_{q_0, q_T, w}(t)) \leq 0, \quad (19)$$

for $t \in [0, T]$ where $C(\cdot)$ is from (17). Throughout, T is set 5. For the parametric trajectory model $q_{q_0, q_T, w}$, we set $B = 20$ thus $w \in \mathbb{R}^{20 \times 7}$.

The optimization variable w is initialized as the zero vector, and η is set to 2. To randomly initialize q_0 and q_T within the joint limits, we first sample two vectors, v_0 and $v_T \in \mathbb{R}^7$, from a standard Gaussian distribution. We then apply the sigmoid function to v_0 and v_T and normalize them using the joint limit values. Empirically, initializing closer to the origin, rather than uniformly across the configuration space, has proven to yield better optimization results. This is likely because uniform initialization can lead to extreme cases, such as the initial q_0 being too close to the target, which can negatively impact the optimization process.

Analysis. We perform and compare trajectory optimizations using two standard constrained optimization algorithms, Sequential Least Squares Programming (SLSQP) [41] and Constrained Optimization BY Linear Approximation (COBYLA) [42], as well as Adaptive moment estimation (Adam) [43], which is widely used in deep learning, focusing on computation times and success rates. When using Adam, an unconstrained optimizer, the inequality constraints are lifted

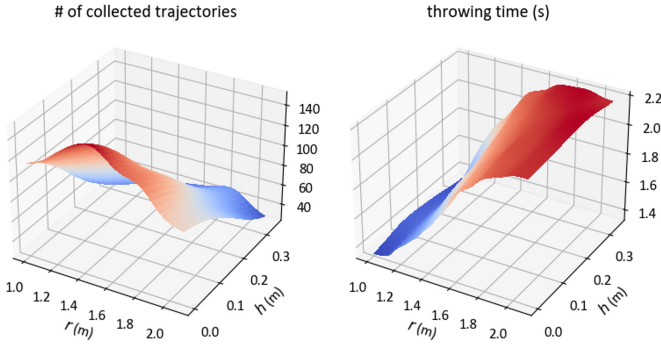


Fig. 8. The number of collected trajectories and throwing times as functions of r and h , where the target box position is $\tau = (r, 0, h)$.

to the objective function by using the ReLU penalty function with a positive weight vector $W \in \mathbb{R}^k$ as in (8):

$$\min_{q_0, q_T, w, \eta} J + \frac{1}{L} \sum_{l=1}^L W^T (\text{ReLU}(C(t_l))^2), \quad (20)$$

where $t_l = \frac{5}{L-1}(l-1)$ ($L = 100$) and $C(t)$ is the left-hand side of (19). The optimizations are terminated when each kinodynamic constraint meets a specific threshold and the position error falls below 0.01. If the number of iterations exceeds 10,000, the optimization is deemed a failure.

Fig. 7 shows the quartiles of the optimization times and convergence rates as functions of $r \in [1.1, 2.0]$, where the target box position is $\tau = (r, 0, 0)$. We ran the optimization ten times for each task parameter, starting with different initializations and seeds, with computations performed on an AMD Milan 2.8 GHz 8-core processor.

Notably, regardless of the solver used, all optimizations take well over 10 seconds, indicating a lengthy process and often failing sensitively depending on the initialization. The Adam optimizer demonstrates the most robust and best results, though it fails in some cases when the distance exceeds 1.7 meters. This outcome highlights the complexity of the nonlinear and nonconvex optimization problem addressed in this case study. While more sophisticated hyperparameter tuning and program optimization could reduce the required time, we believe a significant reduction – such as bringing it down to less than a second, the approximate timescale needed for fast operation – is unlikely.

Data collection. We collect the trajectory dataset by solving the above trajectory optimizations with the Adam optimizer multiple times for each $\tau \in \mathcal{T}_s = \{(r, 0, h) \mid r \in \{1.1, 1.2, \dots, 1.9, 2.0\}, h \in \{0.0, 0.1, 0.2, 0.3\}\}$. For each task parameter, we optimize 300 trajectories, resulting in a total of 12,000 trajectories across 40 candidate task parameters. To speed up data collection, we use a GPU to simultaneously optimize 100 trajectories, summing their objective function values and updating all trajectories concurrently using the gradient descent method. While this approach leads to slightly more failure cases compared to optimizing each trajectory individually, the overall data collection speed is significantly increased due to parallel optimization.

To encourage faster throwing times η , we perform the optimization in (20) with slight modifications. First, we introduce an additional optimization variable, the terminal time T , and include it in the objective function with an appropriate weight. This encourages the optimization to find smaller values for both T and η for the given task. Next, to ensure the terminal time matches the required $T = 5$ for training motion manifold primitives (since our current models require trajectories of the same time length), we adjust the optimized trajectory by trimming it to include only the segment from time 0 to time η . We then append a new trajectory segment that decelerates smoothly to a stop over the remaining time, $5 - \eta$, creating a smooth connection with the original trajectory.

This process produces a total of 3,523 trajectories, with the distribution for each task parameter shown in Fig. 8 (Left). Fig. 8 (Right) illustrates the mean throwing time η as a function of the task parameter. As anticipated, the number of collected trajectories decreases while the throwing time increases as the target position moves farther away.

It is important to note that there is no single method for data collection; the approach should be tailored to the user’s specific needs. However, our current method requires all trajectories to share the same terminal time, which is a limitation. We believe that exploring the use of multiple trajectories with different terminal times is an important direction for future research.

B. Comparisons of Planning Performance

In this section, we compare *Trajectory Optimization (TO)* with the parametric curve models detailed in section V-A, and motion manifold-based methods: *Motion Manifold Primitives (MMP)* with a Gaussian mixture prior [23], *Motion Manifold Flow Primitives (MMFP)* [24], and our *Differentiable Motion Manifold Flow Primitives (DMMFP)*, each of which is trained with a 32-dimensional latent space. To train MMP, MMFP, and DMMFP, we use the same trajectory dataset collected via trajectory optimizations in section V-A. We fine-tune the DMMFP using *Trajectory Manifold Optimization (TMO)* introduced in section IV-D, and denote it by *DMMFP + TMO*. Despite low probability, some generated trajectories by DMMFP + TMO may not meet the required constraints or task goals. Therefore, we use *Rejection Sampling (RS)* to exclude non-compliant samples, denoted by *DMMFP + TMO + RS*, although this step necessitates extra computation to verify the feasibility of the trajectories.

TABLE I presents the averaged Success Rate (SR) – a motion $(q(t), \eta)$ is deemed successful if the position error is less than 0.04 –, Position Error (Error) in meter scale, and Constraint Satisfaction Rates on Joint Limits (JL), Joint Velocity Limits (JVL), Joint Acceleration Limits (JAL), Joint Jerk Limits (JLJ), Cartesian Velocity Limits (CVL), Joint Torque Limits (JTL), and Self-Collisions (COL). A trajectory is considered to satisfy a constraint if it meets the requirement at every time $t \in [0, T]$ along the trajectory. These metrics are computed using both seen task parameters $\tau \in \mathcal{T}_s$ and unseen test task parameters $\tau \in \{(r, 0, h) \mid r \in \{1.15, 1.25, \dots, 1.95\}, h \in \{0.05, 0.15, 0.25\}\}$. The number

TABLE I

AVERAGE SUCCESS RATES, POSITION ERROR, AND VARIOUS CONSTRAINT SATISFACTION RATES. COMPUTATIONS ARE PERFORMED USING AN AMD MILAN 2.8 GHZ 8-CORE PROCESSOR FOR TRAJECTORY OPTIMIZATIONS AND AMD RYZEN 9 5900X 12-CORE PROCESSOR AND NVIDIA GEFORCE RTX 3090 FOR MOTION MANIFOLD PRIMITIVES.

	Seen Task Parameter								Unseen Task Parameter								# Traj.	Time		
	SR	Error	JL	JVL	JAL	JIL	CVL	JTL	COL	SR	Error	JL	JVL	JAL	JIL	CVL			JTL	COL
TO (Adam) [43]	97	0.01	100	100	100	100	100	100	100	100	0.01	100	100	100	100	100	100	100	1	10 ~ 100 s
TO (SLSQP) [41]	33	0.01	100	100	100	100	100	100	100	100	0.01	100	100	100	100	100	100	100	1	10 ~ 3000 s
TO (COBYLA) [42]	66	0.01	100	100	100	100	100	100	100	100	0.01	100	100	100	100	100	100	100	1	100 ~ 1000 s
MMP [23]	1.05	0.53	0.95	0.0	0.0	0.0	0.0	0.0	92.6	0.81	0.53	96.4	0.0	0.0	0.0	0.0	0.0	94.4	100	0.003s
MMFP [24]	77.4	0.05	97.7	0.0	0.0	0.0	0.0	0.0	99.0	15.0	0.15	0.0	0.0	0.0	0.0	0.0	0.0	99.3	100	0.011s
DMMFP	17.5	0.18	99.2	72.5	25.9	100	89.5	64.7	98.6	4.96	0.26	99.4	79.5	32.7	100	93.1	87.4	98.4	100	0.012s
DMMFP + TMO	95.8	0.01	100	93.0	99.9	100	99.9	100	100	94.1	0.02	100	80	98.2	100	100	100	100	100	0.012s
DMMFP + TMO + RS	100	0.01	100	100	100	100	100	100	100	100	0.01	100	100	100	100	100	100	100	91	0.227s

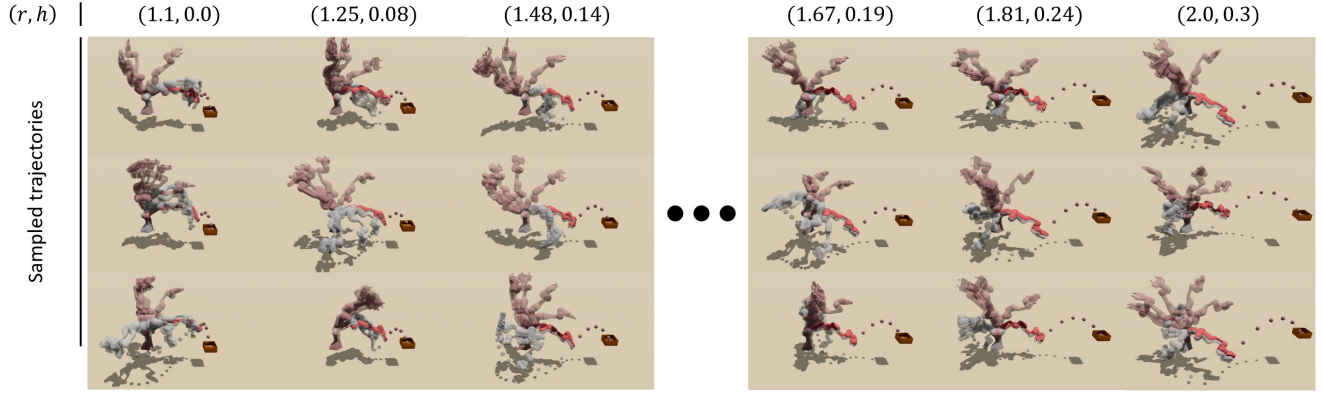


Fig. 9. Examples of diverse generated trajectories by *Differentiable Motion Manifold Primitives (DMMFP) + Trajectory Manifold Optimization (TMO) + Rejection Sampling (RS)* for various task parameters $\tau = (r, 0, h)$. The moment of the throw is depicted in deep red, preceded by gray and followed by transparent red.

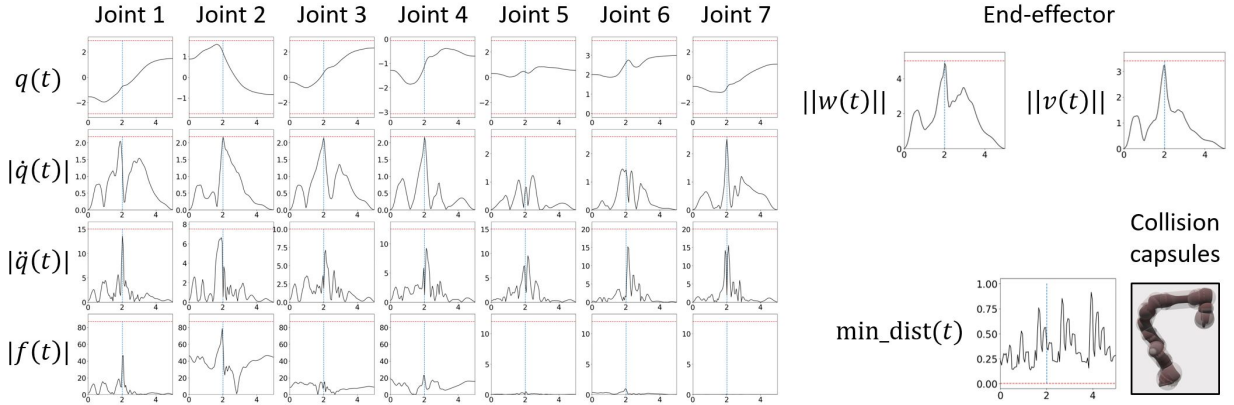


Fig. 10. Trajectories of joint $q(t)$, joint velocity $\dot{q}(t)$, joint acceleration $\ddot{q}(t)$, joint torque $f(t)$, end-effector angular velocity $w(t)$, end-effector linear velocity $v(t)$, and minimum distance between links $\min_dist(t)$ for an example throwing motion generated by *DMMFP + TMO + RS* given the task parameter $\tau = (2.0, 0, 0.3)$. The limit values are visualized as red horizontal lines. The moment of throw is marked in blue vertical lines.

of trajectories generated simultaneously is reported as # Traj. in these experiments, along with the corresponding time consumed.

In this table, we can derive four key findings. First, trajectory optimization is significantly slower than other methods, especially sensitive to initialization, and can take over a minute as the target distance increases, making it impractical for online replanning (see Fig. 7 for more details). In contrast, methods based on the motion manifold are much faster, as neural networks facilitate immediate sampling, even when generating 100 trajectories at once using a GPU. Second, the methods MMP, MMFP, and DMMFP all exhibit low

constraint satisfaction rates, indicating that merely fitting data is inadequate for meeting constraints. DMMFP shows relatively better performance due to the neural network’s inductive bias, which imparts some smoothness along the time axis. Third, through TMO, we observe a significant improvement in DMMFP’s performance. Failures occur occasionally, primarily due to Joint Velocity Limits (JVL). By implementing Rejection Sampling (RS), the success rate can be raised to 100%, with approximately 91 out of 100 samples retained. Lastly, rejection sampling slightly slows down the process due to the need to check the constraints of sampled trajectories; the current implementation took about 0.2 seconds to check 100 trajecto-

ries across 100 equally spaced time grid points. This process involves computing forward kinematics, inverse dynamics, and checking 45 constraints for each of the 100×100 combinations of (q, \dot{q}, \ddot{q}) . It is worth noting that all code is implemented in Python using PyTorch, and the computation time is measured on an AMD Ryzen 9 5900X 12-Core Processor and an NVIDIA GeForce RTX 3090. While this setup may not be fully optimized, using different programming languages could be a potential way to further accelerate the process. Alternatively, training and utilizing a neural network classifier to determine whether a trajectory is feasible could significantly speed up the constraint-checking step.

Diverse throwing motions generated using DMMFP + TMO + RS are visualized in Fig. 9. If there were only a single throwing trajectory, the robot would often have to inefficiently adjust to it, particularly when the current configuration is far from the desired path. In contrast, the diversity in our DMMP approach makes it easier to find a suitable throwing trajectory that closely matches the current configuration. Additionally, an example throwing motion for $\tau = (2.0, 0, 0.3)$ is depicted through graphs of joint angles, velocities, etc., in Fig. 10. In particular, Fig. 10 shows that the robot accelerates to nearly reach the limits of joint velocity and end-effector velocity (red dashed lines) to achieve a longer throw, followed by deceleration. Additionally, peaks in velocity, acceleration, and torque can be observed near the moment of throwing (blue dashed lines).

C. Online Adaptation

In this section, we demonstrate the online adaptability of our model, thanks to its rapid planning speed, in dynamically changing environments. We consider a scenario where, given an initially planned throwing trajectory for a certain target box position and a robot following that trajectory, the target box position suddenly changes. We quickly replan a throwing trajectory, and the robot smoothly and naturally converges to and tracks the new trajectory.

In the replanning step, we first sample multiple throwing trajectories – one hundred in our experiments – denoted by $\{(q_i(t), \eta_i)\}_{i=1}^{100}$, conditioned on the new target box position. Among these trajectories, we select the one that is closest to the current robot configuration q_c – where closeness is measured by the shortest distance to the trajectory segment prior to the release of the object. Specifically, we find $(i^*, t^*) = \arg \min_{(i,t)} \|q_c - q_i(t)\|$ such that $t < \eta_i$. We then compute a transition trajectory that connects the current configuration q_c to the nearest configuration $q_{i^*}(t^*)$, which occurs before the moment of throw, in the selected trajectory.

The transition trajectory starts with the current robot phase (q_c, \dot{q}_c) and ends with the phase $(q_{i^*}(t^*), \dot{q}_{i^*}(t^*))$ from the updated trajectory. We construct the transition trajectory with the following parametric curve model:

$$\begin{aligned} q(t) = & q_0 + (q_T - q_0)(3 - 2s)s^2 \\ & + \dot{q}_0 s - (2\dot{q}_0 + \dot{q}_T)s^2 + (\dot{q}_0 + \dot{q}_T)s^3 \\ & + s^2(s - 1)^2 \Phi(s)w, \end{aligned} \quad (21)$$



Fig. 11. Online adaptation to changes in target box position: A robot follows an initially planned throwing trajectory (red). Before throwing, it detects a change in the target box position, then replans and updates the throwing trajectory (blue), and finds a transition trajectory (gray) that connects the current phase to the updated throwing trajectory.

where $s = t/T$, $\Phi(s) = [\phi_1(s), \dots, \phi_B(s)] \in \mathbb{R}^{1 \times B}$ – where $\phi_i(s) = \exp(-B^2(s - \frac{i-1}{B-1})^2)$ and B is the number of basis functions –, and $w \in \mathbb{R}^{B \times n}$, that is by construction constrained to have phases (q_0, \dot{q}_0) at $t = 0$ and (q_T, \dot{q}_T) at $t = T$. Here, we set $T = 1$. We note this model is slightly more complex than (4) because it requires non-zero initial and terminal velocities.

The transition trajectory must also satisfy kinodynamic constraints, which requires finding a w that results in a trajectory meeting all the constraints. This is a relatively simple problem (assuming no additional obstacles near the robot). Empirically, we found that in most cases, if w is randomly initialized from a standard Gaussian distribution, at least one of the generated trajectories satisfies the constraints. We can then select any suitable w from these options. The entire process is fast enough to be performed online, allowing the robot to adapt to a new trajectory without stopping.

Fig. 11 shows some examples of online adaptation trajectories. On the left, red robots track an initially planned trajectory until a change in the target box position is detected (the target box is moved after 1.8 seconds from the start of the robot’s movement). In the middle, as soon as the target change is detected, gray robots follow the transition trajectory that connects the current robot phase to the nearest phase in the updated trajectory, taking about 1 second. On the right, blue robots follow the updated throwing trajectory, throw the object into the new target box, and come to a stop, taking between 3 to 5 seconds, depending on the distance to the new target.

VI. CONCLUSIONS

We have proposed identifying a trajectory manifold consisting of diverse task-completing trajectories offline, and then performing fast kinodynamic motion planning by searching for a trajectory within the manifold online. We have proposed Differentiable Motion Manifold Primitives (DMMP), a manifold of continuous-time, differentiable trajectories, and a practical training strategy composed of four steps: (i) data collection via trajectory optimizations, (ii) differentiable motion manifold learning, (iii) latent flow learning, and (iv) trajectory manifold optimization. Using dynamic throwing tasks with a 7-DoF robot arm, we have confirmed our method can quickly generate diverse trajectories that satisfy task requirements and kinodynamic constraints.

One of the most important parts of DMMP training is the initial step: data collection via trajectory optimizations. The diversity of this dataset will determine the diversity of the resulting trajectory manifold, which in turn will impact the efficiency of the re-planning algorithm in online adaptation. For example, a manifold with more diverse trajectories is likely to lead to finding a trajectory closer to the robot’s current phase, making it easier to identify a transition trajectory, and leading to reducing both the distance and the time the robot must travel during the transition. In our current implementation, we have collected diverse trajectories through random initializations of the initial and final configurations. Future research directions include using more sophisticated methods to develop a trajectory manifold that spans a broader area.

In this paper, we have demonstrated examples of adaptation when a new task variable is introduced, but our trajectory manifold can also be utilized to adapt to a broader range of scenarios. For instance, in the throwing example, consider a case where additional obstacles, such as a wall, are present near the robot, restricting its workspace. If only a single trajectory had been encoded offline, and that trajectory collided with the additional obstacles, the robot would be unable to throw the object. However, since we have learned a trajectory manifold, we have diverse candidate trajectories, increasing the likelihood of finding a trajectory on the manifold that avoids collisions with the obstacles. As mentioned earlier, to achieve higher adaptability, it is important to learn a manifold that includes as many diverse trajectories as possible.

REFERENCES

- [1] B. Donald, P. Xavier, J. Canny, and J. Reif, “Kinodynamic motion planning,” *Journal of the ACM (JACM)*, vol. 40, no. 5, pp. 1048–1066, 1993.
- [2] D. J. Webb and J. Van Den Berg, “Kinodynamic rrt*: Asymptotically optimal motion planning for robots with linear dynamics,” in *2013 IEEE international conference on robotics and automation*. IEEE, 2013, pp. 5054–5061.
- [3] L. Chen, I. Mantegh, T. He, and W. Xie, “Fuzzy kinodynamic rrt: a dynamic path planning and obstacle avoidance method,” in *2020 international conference on unmanned aircraft systems (ICUAS)*. IEEE, 2020, pp. 188–195.
- [4] S. Karaman and E. Frazzoli, “Optimal kinodynamic motion planning using incremental sampling-based methods,” in *49th IEEE conference on decision and control (CDC)*. IEEE, 2010, pp. 7681–7687.
- [5] J. Schulman, Y. Duan, J. Ho, A. Lee, I. Awwal, H. Bradlow, J. Pan, S. Patil, K. Goldberg, and P. Abbeel, “Motion planning with sequential convex optimization and convex collision checking,” *The International Journal of Robotics Research*, vol. 33, no. 9, pp. 1251–1270, 2014.
- [6] R. Bonalli, A. Cauligi, A. Bylard, and M. Pavone, “Gusto: Guaranteed sequential trajectory optimization via sequential convex programming,” in *2019 International conference on robotics and automation (ICRA)*. IEEE, 2019, pp. 6741–6747.
- [7] D. Malyyuta, T. P. Reynolds, M. Szmuk, T. Lew, R. Bonalli, M. Pavone, and B. Açıkmeşe, “Convex optimization for trajectory generation: A tutorial on generating dynamically feasible trajectories reliably and efficiently,” *IEEE Control Systems Magazine*, vol. 42, no. 5, pp. 40–113, 2022.
- [8] M. N. Pivtoraiko, “Differentially constrained motion planning with state lattice motion primitives,” Ph.D. dissertation, Carnegie Mellon University, The Robotics Institute, 2012.
- [9] B. Sakcak, L. Bascetta, G. Ferretti, and M. Prandini, “Sampling-based optimal kinodynamic planning with motion primitives,” *Autonomous Robots*, vol. 43, no. 7, pp. 1715–1732, 2019.
- [10] J. Park, S. Karumanchi, and K. Iagnemma, “Homotopy-based divide-and-conquer strategy for optimal trajectory planning via mixed-integer programming,” *IEEE Transactions on Robotics*, vol. 31, no. 5, pp. 1101–1115, 2015.
- [11] M. Kuderer, C. Sprunk, H. Kretschmar, and W. Burgard, “Online generation of homotopically distinct navigation paths,” in *2014 IEEE International Conference on Robotics and Automation (ICRA)*. IEEE, 2014, pp. 6462–6467.
- [12] A. Perez, R. Platt, G. Konidaris, L. Kaelbling, and T. Lozano-Perez, “Lqr-rrt*: Optimal sampling-based motion planning with automatically derived extension heuristics,” in *2012 IEEE International Conference on Robotics and Automation*. IEEE, 2012, pp. 2537–2542.
- [13] M. Yavari, K. Gupta, and M. Mehrandezh, “Lazy steering rrt*: An optimal constrained kinodynamic neural network based planner with no in-exploration steering,” in *2019 19th International Conference on Advanced Robotics (ICAR)*. IEEE, 2019, pp. 400–407.
- [14] P. Atreya and J. Biswas, “State supervised steering function for sampling-based kinodynamic planning,” *arXiv preprint arXiv:2206.07227*, 2022.
- [15] A. H. Qureshi, J. Dong, A. Baig, and M. C. Yip, “Constrained motion planning networks x,” *IEEE Transactions on Robotics*, vol. 38, no. 2, pp. 868–886, 2021.
- [16] A. H. Qureshi, Y. Miao, A. Simeonov, and M. C. Yip, “Motion planning networks: Bridging the gap between learning-based and classical motion planners,” *IEEE Transactions on Robotics*, vol. 37, no. 1, pp. 48–66, 2020.
- [17] O. Von Stryk and R. Bulirsch, “Direct and indirect methods for trajectory optimization,” *Annals of operations research*, vol. 37, pp. 357–373, 1992.
- [18] A. J. Ijspeert, J. Nakanishi, H. Hoffmann, P. Pastor, and S. Schaal, “Dynamical movement primitives: learning attractor models for motor behaviors,” *Neural computation*, vol. 25, no. 2, pp. 328–373, 2013.
- [19] S. M. Khansari-Zadeh and A. Billard, “Learning stable nonlinear dynamical systems with gaussian mixture models,” *IEEE Transactions on Robotics*, vol. 27, no. 5, pp. 943–957, 2011.
- [20] A. Paraschos, C. Daniel, J. R. Peters, and G. Neumann, “Probabilistic movement primitives,” *Advances in neural information processing systems*, vol. 26, 2013.
- [21] M. Saveriano, F. J. Abu-Dakka, A. Kramerberger, and L. Peternel, “Dynamic movement primitives in robotics: A tutorial survey,” *arXiv preprint arXiv:2102.03861*, 2021.
- [22] M. Noseworthy, R. Paul, S. Roy, D. Park, and N. Roy, “Task-conditioned variational autoencoders for learning movement primitives,” in *Conference on robot learning*. PMLR, 2020, pp. 933–944.
- [23] B. Lee, Y. Lee, S. Kim, M. Son, and F. C. Park, “Equivariant motion manifold primitives,” in *7th Annual Conference on Robot Learning*, 2023.
- [24] Y. Lee, B. Lee, S. Kim, and F. C. Park, “Motion manifold flow primitives for language-guided trajectory generation,” *arXiv preprint 2407.19681*, 2024.
- [25] Y. Zhou, J. Gao, and T. Asfour, “Learning via-point movement primitives with inter-and extrapolation capabilities,” in *2019 IEEE/RSJ International Conference on Intelligent Robots and Systems (IROS)*. IEEE, 2019, pp. 4301–4308.
- [26] P. Kicki, P. Liu, D. Tateo, H. Bou-Ammar, K. Walas, P. Skrzypczyński, and J. Peters, “Fast kinodynamic planning on the constraint manifold with deep neural networks,” *IEEE Transactions on Robotics*, 2023.
- [27] Y. Lee, “Mmp++: Motion manifold primitives with parametric curve models,” *IEEE Transactions on Robotics*, 2024.
- [28] G. Arvanitidis, L. K. Hansen, and S. Hauberg, “Latent space oddity: on the curvature of deep generative models,” *arXiv preprint arXiv:1710.11379*, 2017.

- [29] Y. Lee, H. Kwon, and F. Park, "Neighborhood reconstructing autoencoders," *Advances in Neural Information Processing Systems*, vol. 34, pp. 536–546, 2021.
- [30] Y. Lee, S. Kim, J. Choi, and F. Park, "A statistical manifold framework for point cloud data," in *International Conference on Machine Learning*. PMLR, 2022, pp. 12 378–12 402.
- [31] Y. Lee, S. Yoon, M. Son, and F. C. Park, "Regularized autoencoders for isometric representation learning," in *International Conference on Learning Representations*, 2022.
- [32] C. Jang, Y. Lee, Y.-K. Noh, and F. C. Park, "Geometrically regularized autoencoders for non-euclidean data," in *The Eleventh International Conference on Learning Representations*.
- [33] Y. Lee, "A geometric perspective on autoencoders," *arXiv preprint arXiv:2309.08247*, 2023.
- [34] Y. Lee and F. C. Park, "On explicit curvature regularization in deep generative models," in *Topological, Algebraic and Geometric Learning Workshops 2023*. PMLR, 2023, pp. 505–518.
- [35] J. Lim, J. Kim, Y. Lee, C. Jang, and F. C. Park, "Graph geometry-preserving autoencoders," in *Forty-first International Conference on Machine Learning*.
- [36] D. P. Kingma and M. Welling, "Auto-encoding variational bayes," *arXiv preprint arXiv:1312.6114*, 2013.
- [37] Y. Lipman, R. T. Chen, H. Ben-Hamu, M. Nickel, and M. Le, "Flow matching for generative modeling," *arXiv preprint arXiv:2210.02747*, 2022.
- [38] J. J. Park, P. Florence, J. Straub, R. Newcombe, and S. Lovegrove, "DeepSDF: Learning continuous signed distance functions for shape representation," in *Proceedings of the IEEE/CVF conference on computer vision and pattern recognition*, 2019, pp. 165–174.
- [39] L. Lu, P. Jin, and G. E. Karniadakis, "Deeponet: Learning nonlinear operators for identifying differential equations based on the universal approximation theorem of operators," *arXiv preprint arXiv:1910.03193*, 2019.
- [40] R. T. Chen, Y. Rubanova, J. Bettencourt, and D. K. Duvenaud, "Neural ordinary differential equations," *Advances in neural information processing systems*, vol. 31, 2018.
- [41] D. Kraft, "A software package for sequential quadratic programming," *Forschungsbericht- Deutsche Forschungs- und Versuchsanstalt für Luft- und Raumfahrt*, 1988.
- [42] M. J. Powell, *A direct search optimization method that models the objective and constraint functions by linear interpolation*. Springer, 1994.
- [43] D. P. Kingma and J. Ba, "Adam: A method for stochastic optimization," *arXiv preprint arXiv:1412.6980*, 2014.